Robust trajectory optimisation of a TSTO spaceplane using uncertainty-based atmospheric models

Lorenzo Ricciardi, Christie Maddock* and Massimilano Vasile
Aerospace Centre of Excellence, University of Strathclyde, Glasgow, United Kingdom

This paper presents a multi-objective trajectory optimisation under uncertainty for the ascent of a two-stage, semi-reusable space launch system. Using Orbital Access' Orbital 500-R launcher as a test case, robust multi-disciplinary design optimisation is used to analyse the trade-offs with both the vehicle and system design, and operation. An area of focus is on the predicted performance and its impact on the design and planned mission scenarios. The atmospheric model uncertainties are quantified for the atmospheric surrogate model and integrated into the optimal control solver MODHOC, extended by the addition of an unscented transformation to handle the uncertainties. A multi-objective optimisation under uncertainty is run, examining the Pareto-optimal sets for the ascent trajectory and vehicle design.

I. Introduction

Uncertainty quantification (UQ) is the science of quantifying the uncertainties within the predicted performance of a system. At system level, UQ analysis can translate into the assessment of the whole system reliability or the reliability of one or more components. An uncertainty quantification analysis is, therefore, a fundamental step towards de-risking any technological solution as it provides a quantification of the variation in performance and probability of recoverable or unrecoverable system failures, given existing information.

Integrating UQ into the optimisation process leads to, generally, two types of multi-disciplinary design optimisation: reliability-based design optimisation (RBDO) which finding an optimal design with low probability of failure, and robust design optimisation (RDO) which aims to reduce the variability of the system performance. [1, 2] Within the industrial development, RDO is being applied to the Orbital 500-R, an air launched, two-stage-to-orbit semi-reusable launch system under design by Orbital Access Ltd. [3–5]

The current project assesses the robustness of the guidance trajectory design of the full mission considering the uncertainty related to the atmospheric models. Given the early stage of the vehicle design and the wide scope of use required by the commercial side, a number of mission scenarios are possible, each of which is affected differently by the same sets of uncertainties.

In this paper, we present results for the design of the ascent trajectories and vehicle sizing, optimising a two objectives, minimisation of the gross vehicle mass and minimisation of effect of the uncertainty on the performance, for a nominal mission of delivering a 500 kg payload to a circular 650 km polar orbit.

II. Robust design optimisation

A. Multi-objective optimal control

MODHOC*, Multi-Objective Direct Hybrid Optimal Control solver [6, 7], is based on a Direct Finite Elements Transcription (DFET) of the optimal control problem [8] and a solution of the transcribed problem with a multi-agent, multi-objective optimisation algorithm (MACS) [9]. By combining MACS and DFET, MODHOC has the ability to perform a global exploration of the solution space and to converge locally to optimal solutions. It works for arbitrarily connected multi-phase problems with general dynamics, and ensures an even spread set of solutions within the Pareto-optimal set. The software has been successfully used for the trajectory and design optimisation of vertical and horizontal launch systems [10, 11], deployment of constellations [12], interplanetary exploration missions [13] and the design of multi-debris removal missions.

*Corresponding author: christie.maddock@strath.ac.uk

*Open-source code available on github under SMART-O2C, Strathclyde Mechanical and Aerospace Research Toolbox for Optimisation and Optimal Control, `https://github.com/strath-ace/smart-o2c`

B. Optimisation under uncertainty

To account for model uncertainty, the optimal control solver MODHOC was extended to include an Square Root Unscented Transformation in the formulation of the optimal control problem [14].

Unscented Transformations capture the first statistical moments, mean and covariance, of the distributions of the states of a system subject to uncertainty and undergoing arbitrary non-linear transformations by propagating a number of sigma points $\boldsymbol{\chi}$. If the system depends on N_{uq} uncertain variables, whose mean and covariances are known, the unscented transformation requires the propagation of $(2N_{uq} + 1)$ sigma points, or samples. The first sigma point takes the mean value of all the uncertain variables, while the others assume the mean plus (or minus) the square root of the matrix of the covariances of the uncertain variables. All the sigma points are propagated simultaneously with the mean and covariance of the final states computed as a weighted combination of the final states of each sigma point.

The approach employed follows that of Ross et al. [15]. Let the dynamics of the systems be given by

$$\dot{\mathbf{x}} = \mathbf{F}(\mathbf{x}, \mathbf{u}, \mathbf{b}_{uq}, t) \tag{1}$$

where $\mathbf{x}$ are the states of the system, $\mathbf{u}$ are the controls, t is time, and $\mathbf{b}_{uq}$ are additional static parameters affected by uncertainty. The dynamics for each sigma point $\boldsymbol{\chi}_i$ is therefore,

$$\dot{\boldsymbol{\chi}}_i = \mathbf{F}(\boldsymbol{\chi}_i, \mathbf{u}, \mathbf{b}_i, t) \quad \text{for } i = 1, \ldots, (2N_{uq} + 1) \tag{2}$$

As each sigma point has a different value for the static uncertain variables, the dynamics evolve independently of the other sigma points. All sigma points however are controlled by the same control law. The goal is to find a single control law that, when applied to all sigma points, allows the set of resulting trajectories to all reach the desired final conditions, and to be optimal in some sense. The particular values for the static variables at each sigma point $\mathbf{b}_i$ is decided by the application of the Unscented Transformation.

A known problem of the Unscented Transformation is that it can generate covariance matrices that are not semidefinite positive. To avoid this problem, a Square Root Unscented Transformation [16] was implemented. Algorithmically it is very similar to the standard UT, but it differs in the method used to generate the sigma points. The sigma points are computed using the Cholesky factorisation of the covariance matrix, and slightly different algebraic manipulations are performed to obtain the covariance matrix of the transformed states. This has the advantage that the resulting covariance matrix is guaranteed to be semi-definite positive (up to machine precision).

Mathematically, the problem can be described as follows. Let $\boldsymbol{X}$ be a state vector of length $N_\sigma N_x$,

$$\mathbf{X} := \left[\boldsymbol{\chi}_0, \boldsymbol{\chi}_1, \cdots, \boldsymbol{\chi}_{N_\sigma}\right]^T \tag{3}$$

where N_σ is the number of sigma points, and N_x is the number of states. The dynamics of this system are given by,

$$\mathbf{X} = \begin{bmatrix} \mathbf{f}(\boldsymbol{\sigma}_0, \mathbf{u}, \mathbf{b}_0, t) \\ \mathbf{f}(\boldsymbol{\sigma}^1, \mathbf{u}, \mathbf{b}_1, t) \\ \vdots \\ \mathbf{f}(\boldsymbol{\sigma}_{N_\sigma} \mathbf{u}, \mathbf{b}_{N_\sigma}, t) \end{bmatrix} := \mathbf{F}(\mathbf{X}, \mathbf{u}, \mathbf{B}, t) \tag{4}$$

where B is the vector of uncertain parameters. The multi-objective unscented optimal control problem can thus be formulated as,

$$\begin{aligned} &\min_{\mathbf{u} \in U} \mathbf{J}(\mathbf{X}, \mathbf{u}, \mathbf{B}, t) \\ &s.t. \\ &\dot{\mathbf{X}} = \mathbf{F}(\mathbf{X}, \mathbf{u}, \mathbf{B}, t) \\ &\mathbf{g}(\mathbf{X}, \mathbf{u}, \mathbf{B}, t) \geq 0 \\ &\boldsymbol{\psi}(\mathbf{X}(t_0), \mathbf{X}(t_f), \mathbf{u}(t_0), \mathbf{u}(t_f), \mathbf{B}, t_0, t_f) \geq 0 \\ &t \in [t_0, t_f] \end{aligned} \tag{5}$$

where $\mathbf{g}$ and $\boldsymbol{\psi}$ are the inequality constraints for the path and boundary respectively.

III. Test case

The robust design optimisation was applied to the Orbital-500R launch system, in particular the powered, two-stage ascent. Previous work has looked at understanding the impact of key vehicle and system design parameters (not including any uncertainty) [4, 17], and the effect of uncertainty on the unpowered re-entry of the first stage [14].

A. Launch system models

The Orbital-500R system is composed of a first stage reusable spaceplane, capable of rocket-powered ascent and an unpowered, glided descent, and an expendable, rocket-based upper stage housed internally (see Fig. 1). The spaceplane has a length of 19.5 m, fuselage width of 3.6 m, and a wing span of 12.6 m.

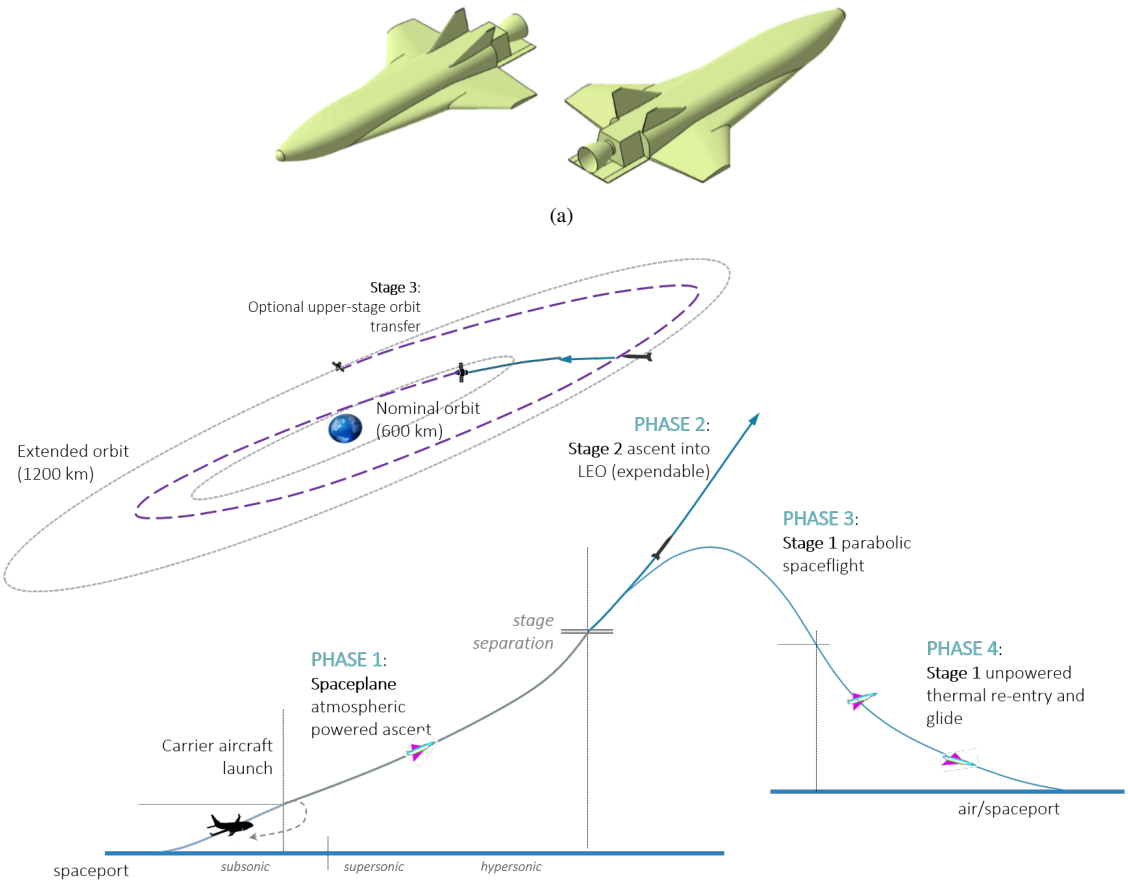

Fig. 1 Orbital 500-R launch vehicle and operations

The primary mission of the Orbital 500-R system is to deliver payloads up to 500 kg to a 650 km circular orbit at an inclination of 88.2 deg. The secondary extended mission is to deliver payloads to a maximum altitude of 1200 km with payloads up to 150 kg. These mission parameters derive from investigations during the previous Future Small Payload Launcher UK study, with the goal of establishing the Orbital 500-R as a commercial logistics system for in-orbit delivery. [5, 18]

The flight dynamics are modelled as a variable-mass point with three degrees of freedom in the Earth-Centered Inertial (ECI) reference frame [19], subject to gravitational, aerodynamic lift and drag forces. The state vector $\mathbf{x}$ contains the time-varying translational flight dynamics, expressed in ECI (and Earth-Centered-Earth-Fixed, ECEF), plus the vehicle mass.

$$\mathbf{x}(t, \mathbf{u}) = [\mathbf{r}, \mathbf{v}, m] = [h,\ \lambda,\ \theta,\ v,\ \gamma,\ \chi, m] \tag{6}$$

$$\mathbf{u}(t) = [\tau, \alpha, \mu] \tag{7}$$

where h is the altitude, (λ, θ) are the geodetic latitude and longitude, v is the magnitude of the relative velocity vector directed by the flight path angle γ and the flight heading angle χ, and $m(t)$ is the time-varying vehicle mass. The vehicle is controlled through an open-loop control vector $\mathbf{u}$ directing the net thrust vector, where τ is the fraction applied of the maximum available thrust, α, μ are the the angle of attack and bank angle of the vehicle. The Earth is modelled as a perfect sphere of radius R_E, rotational velocity ω_E and a gravitational constant μ_E.

The aerodynamic lift and drag coefficients were modelled using an artificial neural network trained using an aerodynamic database for the coefficients of lift and drag using numerical simulations of differing fidelity, e.g., panel methods and CFD solvers such as SU2, ANITA and ANSYS Fluent [20].

B. Uncertainty model for atmospheric parameters

Analysis to date on the design of the Orbital 500-R has employed the US-76 Standard atmospheric model [21]. The US-76 is a global static standard model, giving the atmospheric temperature T and density ρ, and atmospheric pressure, as function of altitude up to 1000 km.

In order to assess the robustness of the design against uncertainties in the atmospheric model, a uncertainty model for the US-76 was developed. A comparison was made against a higher fidelity atmospheric model, NRLMSISE-00 [22]. NRLMSISE-00 is an empirical, global reference atmospheric model primary used to model atmospheric drag for satellite orbital decay, or fly-by manoeuvres. Unlike US-76 that is a function only of altitude, NRLMSISE-00 has eight inputs accounting for seasonal, geographic, solar and magnetic effects: Mean Julian Date (MJD2000), geodetic altitude (also up to 1000 km), latitude, longitude, local apparent solar time, 81-day average of F10.7 solar flux, daily F10.7 solar flux for previous day, and daily magnetic index.

A statistical analysis was performed treating the NRLMSISE-00 input parameters as uncertain. This allowed a measure of the uncertainty of the atmospheric temperature and density as a function of altitude, in order to compare against the nominal US-76 model. A low discrepancy Halton sequence was used to generate 10^5 samples, which were fed into the NRLMSISE-00 model for all altitudes in the range between 0 and 100 km. To account for the possible differences between the models, the relative average difference between the values of the two model was computed for all the thermodynamic quantities. These relative errors, shown in Figure 2 were then treated as random fluctuations, for which averages and covariances were computed as a function of altitude.

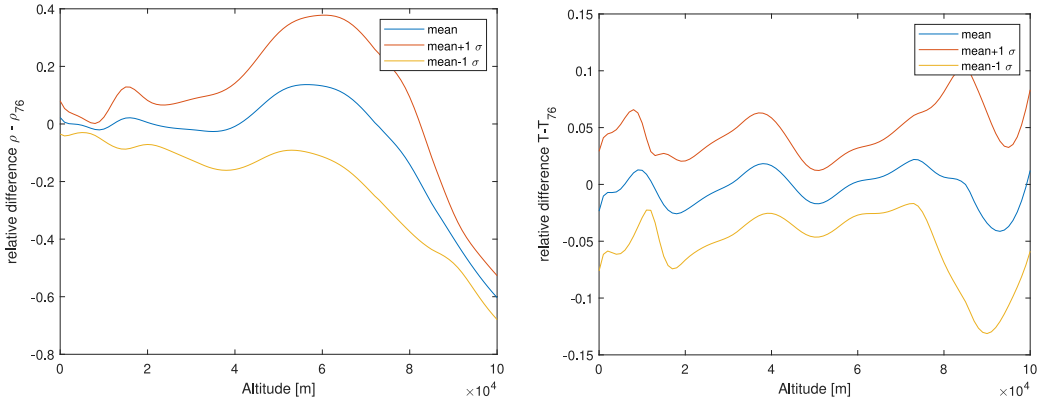

(a) Density (b) Temperature

Fig. 2 Relative error on the atmospheric parameters

The mean relative errors for the atmospheric temperature are very low, with a 1σ relative error around 5% for altitudes below 80 km. The mean relative errors for density are also small for relatively low altitudes, below ~40 km but increase at higher altitudes where the 1σ bands are much wider. Above 50 km the density has a very low absolute value, 10^{-5} kg/m^3, so a large relative error still means a low absolute error. It is thus expected that the impact of these relatively high differences in density between the two models will not affect significantly the initial ascent of the trajectory.

To work within the Square Root Unscented Transformation, different models were generated: one employing the mean relative error, and others adding the Cholesky factorisation of the covariance matrix of the uncertain quantities at each altitude. The resulting curves for temperature as a function of time are plotted on Figure **??**.

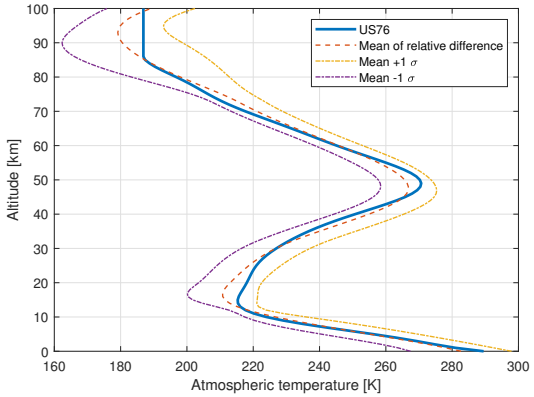

Fig. 3 Temperature profiles for the US76 model (nominal), plus the uncertainty model mean and standard deviation

C. Optimisation configuration

The vehicle is air dropped at an altitude of 10 km, a velocity of 200 m/s and a flight path angle of 10 deg, on an equatorial east-bound trajectory. The final conditions are expressed as difference between the mean and the target value,

$$\boldsymbol{\psi}(\mathbf{X}(t_f)) = \boldsymbol{\mu}_{\chi} - \overline{x}(t_f) = 0 \tag{8}$$

where $\boldsymbol{\mu}_{\chi}$ is the mean of the final states of the sigma points, and $\overline{x}(t_f)$ is the target value. The final conditions imposed on the second stage were to reach a circular equatorial orbit at an altitude of 650 km, delivering a payload of 500 kg. The final orbit was constrained to match the semi-major axis, the eccentricity and the inclination, with the argument of perigee, right ascension of the ascending node, and true anomaly left free.

The optimisation vector is composed of the the discrete flight control law $[\alpha_j, \tau_j, \Delta t]$ for $j = 1, \ldots, N_C$ control nodes and a time of flight $\Delta t = t_f - t_0$, and a set of static vehicle design variables $[T_{1,vac}, T_{2,vac}, m_0]$, where T_{vac} is the vacuum thrust rating for the propulsion system for Stages 1 and 2, and m_0 is the gross mass of vehicle. A mass model for the vehicle was developed that calculated the dry mass of each stage, sizing the propellant tanks and engine system mass as a function of the propellant mass m_p and T_{vac} determined by the optimisation.

The first objective is the minimisation of the initial vehicle mass,

$$J_1 := m(0) \tag{9}$$

The second objective is meant to reduce the uncertainty of the final state. To this end, the sum of the square of all the entries of the covariance matrix of the final states is minimised.

$$J_2 := \sum_{i,j} \left(\mathrm{cov}_{i,j}(\mathbf{X}(t_f))\right)^2 \tag{10}$$

where $\mathrm{cov}_{i,j}$ is computed in the Square Root Unscented Transformation, with the additional consideration that no update of the Cholesky factorisation is needed since no measurement is performed and thus no error is present. This formulation has the advantages that the quantity is smooth and differentiable, involves all components of the covariance matrix, and does not require iterative procedures like decomposition in eigenvalues to compute the principal axes of the ellipsoid of the uncertainty. In order to give each element of the covariance matrix the same weight even if the quantities of interest have different scales, the state variables were scaled by the same factors internally employed by MODHOC to ensure that all variables assume values between 0 and 1.

The problem was discretised with 3 elements of order 7 for each phase, for a total of 1893 variables for the inner-level and single level problem, and 143 for the outer-level problem.

IV. Results and discussion

MODHOC was run with 10 agents, looking for 10 points on the Pareto front.

Figure 4a shows the resulting Pareto front: as evident, there is significant trade-off between the minimum gross initial mass, which varies between approximately 48 t and 62 t, and the minimum final state uncertainty, which varies between 1×10^{-12} and 1×10^{-4}. In addition, the Pareto front appears to be L-shaped with a very sharp slope change, indicating that it is possible to obtain a significant reduction in final uncertainty with a few percents increase of the initial mass (Solutions 6 to 10). A marginal further reduction in uncertainty is possible, but is marginal and requires a significant mass penalty (Solutions 1 to 5). The points on the Pareto front are not uniformly spread, thus it is expected that a higher number of function evaluations or more points on the front could reveal additional features.

Figure 4b shows the time history of the total mass. Mass is the only state variable that is not subject to uncertainty, as it depends only on the throttle, which is a control variable and is known without uncertainty. This would not be true if the specific impulse of the engines were not constant for each phase, as in this case, but dependant on the uncertain atmospheric properties.

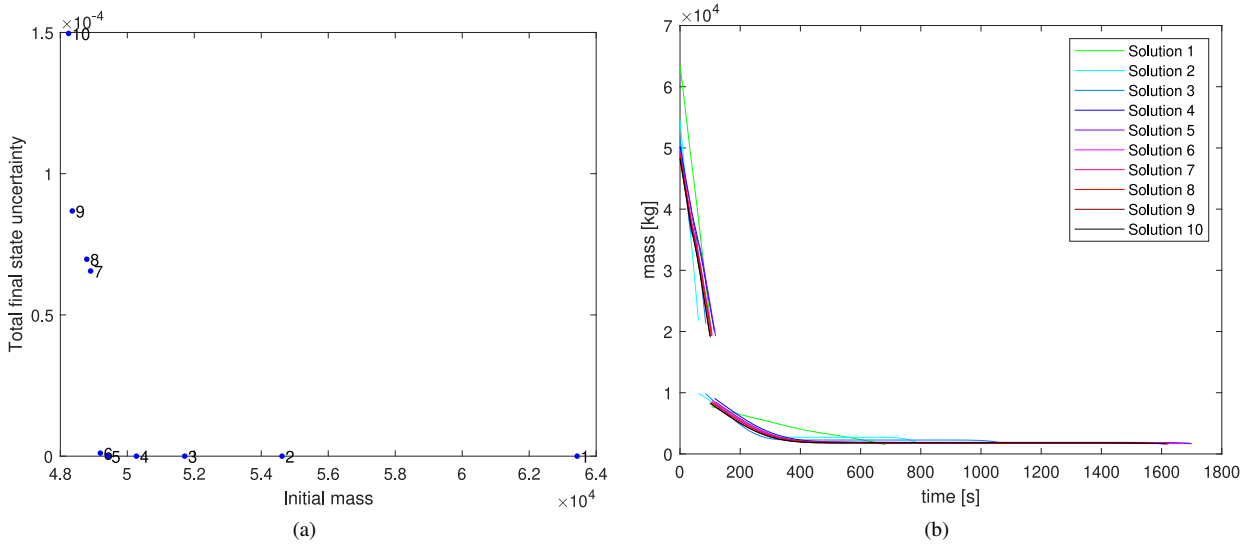

Fig. 4 a) Pareto front b) time history of the mass for each of the 10 solutions in the Pareto front in Fig. 4a.

Figure 5a shows the time history of altitude: for each solution, the average is plotted with a continuous line, the 1σ confidence interval with a dashed dotted line, and the individual trajectories of each sigma point is plotted with a dotted line. This figure not only shows the difference in dispersion between the solutions privileging robustness instead of performance, but also that robust solutions tend to have a shorter mission time, in particular solutions 1 to 3. This is reasonable from a physical point of view, as longer mission times allow uncertainty to grow. In addition, since density decreases very quickly as the altitude increases, the atmospheric model only has an effect on the first part of the trajectory, thus there is a likely benefit in leaving the uncertain region as quickly as possible.

Figure 5b shows the standard deviation of the altitude as a function of time, and allows to compare the difference in dispersion at the final time. In particular, solution 1 has a final standard deviation of altitude of approximately 400 m, while solution 10 has a standard deviation of approximately 86 km, which is 215 times higher. Although this difference can seem staggering, it must be remembered that these are open loop solutions, with no navigation or feedback control to track a reference guidance, thus it should be no surprise that the uncertainties can become so large. Nevertheless, the most robust control profile is able to produce a robust solution, with a much lower expected final state error, even without sensors and a feedback control loop.

Figure 6 shows the time history of the altitude, restricted to Solutions 5 to 10, and without showing the trajectories of the individual sigma points. These solutions have a stronger emphasis on the reduction of the initial mass, and exhibit a similar profile. However, this figure allows to better appreciate the possibility of having a significant reduction in final state uncertainty while maintaining a certain level of performances.

With the same plot coding as Figure 5, Figure 7a shows the time histories of the velocities. This figure shows a qualitative difference in the acceleration profile between solution 1 and all the others, while solutions 2 and 3 are more similar to the rest, although their total mission time is shorter. This difference will be investigated in more detail later on. Figure 7b shows the time history of the standard deviation of velocity. As in the previous case, there is a significant

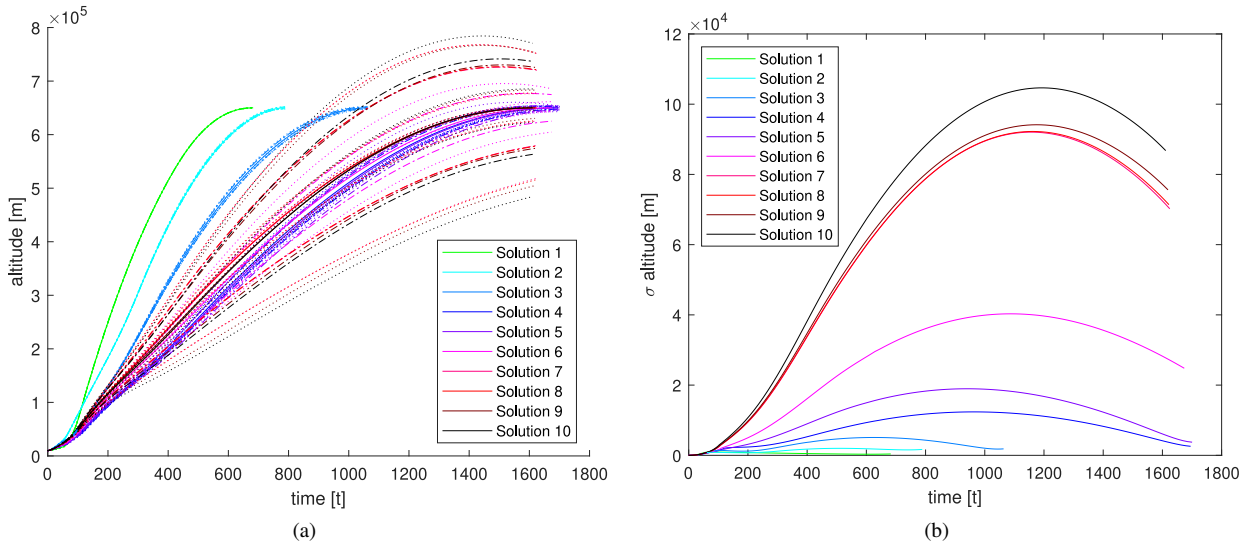

Fig. 5 Time-history of a) the altitude and b) its standard deviation, for each of the 10 solutions in the Pareto front in Fig. 4a.

difference between solution 1, which has a final time standard deviation of approximately 10 m/s, and solution 10, with approximately 150 m/s.

Figure 8a and 8b show the time history for the flight path angle and its standard deviation. For all solutions the maximum standard deviation of the flight path angle appears to be towards the beginning of the mission. This seems reasonable as the flight path angle depends on the aerodynamic forces and primarily on air density, which is an uncertain atmospheric variable.

Figure 10a shows the time history for the axial acceleration, while Figure 9b shows its standard deviation. Solutions 1 to 3 show the highest accelerations, again supporting the hypothesis that it is beneficial to leave the atmosphere as quickly as possible, and to have the shortest overall mission time possible. The values of axial acceleration are all below 7.5g even if no threshold was imposed. From Solution 2 on, it is possible to see the presence of a region with almost zero axial accelerations, indicating a coasting arc. This is consistent with the expected and well known result for mass minimisation of space launch vehicles. Uncertainties for this acceleration appear to be very contained, and barely visible in Figure 9a. Also in this case, the highest uncertainties are encountered in the atmospheric stage.

Figure 10a and 10b show the time history for the normal accelerations. Similar conclusions to the axial accelerations can be made. However, in the atmospheric phase, the uncertainty for this acceleration is one order of magnitude larger than for the axial acceleration. This is reasonable as normal accelerations are almost entirely governed by aerodynamic forces, which are uncertain.

The total effect of the accelerations, the magnitude of the acceleration vector, is shown in Figure 11a and Figure 11b.

Figure 12a and 12b show the time history of the dynamic pressure, and its uncertainty. It is possible to notice that while Solutions 3 to 10 exhibit a very similar profile, with a reasonable peak around 30 kPa, Solution 1 and 2 have instead a much higher value. This again indicates that in order to reduce the uncertainties for the final state, the optimiser found that the most effective strategy is to leave the atmosphere as quickly as possible, increasing the peak dynamic pressure.

Finally, Figure 13a and 13b show the time history for the controls. The throttle profile confirms that solutions privileging minimum mass exhibit a coast arc, which gets shorter as the resulting uncertainty in the final state decreases. For solution 1, which minimises the uncertainty, the engine is always operating, again confirming that reducing the total mission time helps in reducing the final time uncertainty.

V. Conclusions

A multi-objective robust design and trajectory optimisation was conducted on the Orbital-500R vehicle. An uncertainty model was developed for the atmospheric model. By employing the multi-objective hybrid optimal control

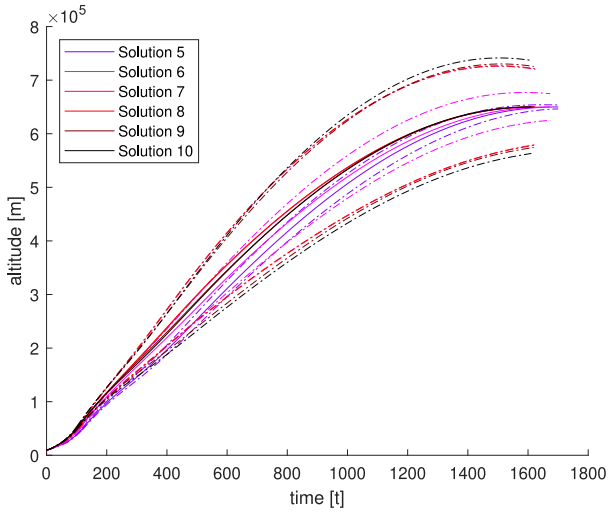

Fig. 6 Time history of the altitude, only for Solutions

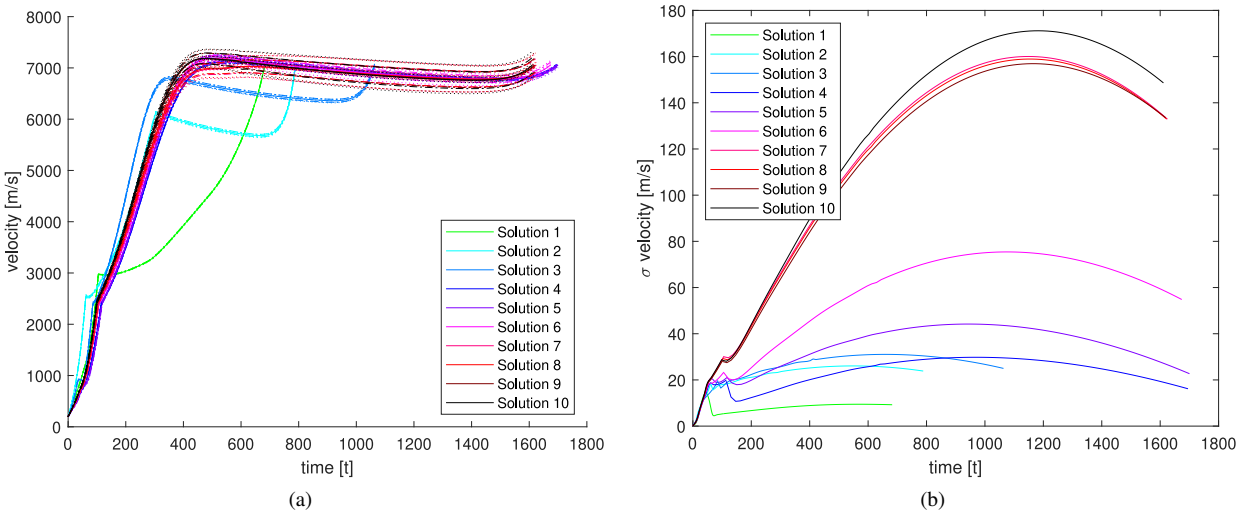

Fig. 7 Time-history of a) the velocity and b) its standard deviation, for each of the 10 solutions in the Pareto front in Fig. 4a.

solver MODHOC and the Unscented Transformation, it was possible to generate several trade-off designs achieving a different balance between performances, measured by the minimisation of the initial mass to deliver a given payload at a target altitude, and the robustness of the solution, measured by the covariance of the final states. Next steps are to develop a more comprehensive quantification of the uncertainty of the atmospheric model, aerodynamic models, and on the initial conditions. These will optimised for the full mission, a branched trajectory from carrier release to orbit (Stage 2) and landing (Stage 1).

Acknowledgements

This work has been partially funded by the UK Space Agency and European Space Agency (ESA) General Support Technology Programme (GSTP) De-Risking Call 2017/18, ESA RFP/2-1690/18/NL/BJ/zk.

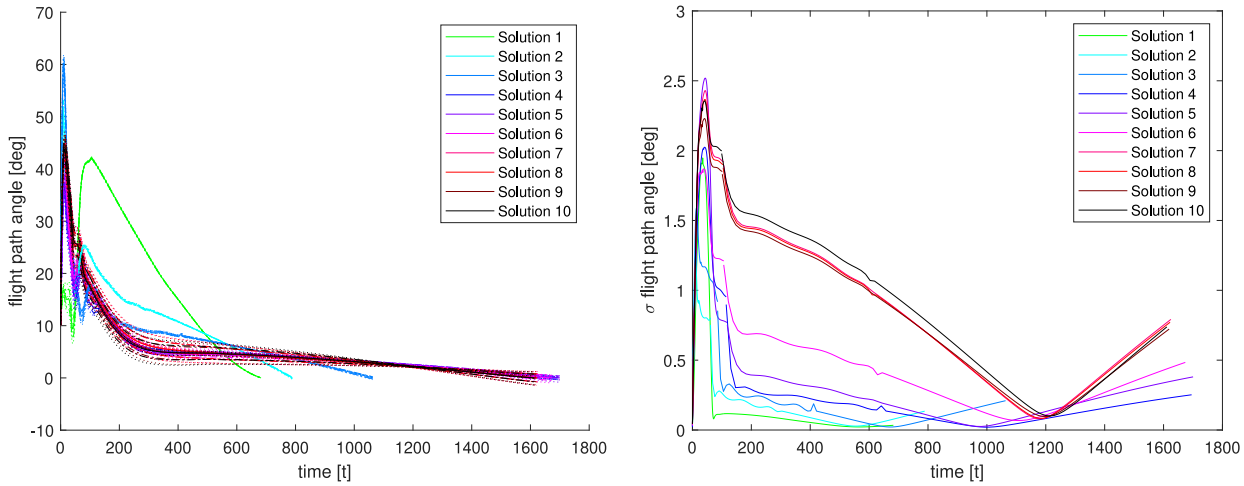

(a) (b)

Fig. 8 Time-history of a) the flight path angle and b) its standard deviation, for each of the 10 solutions in the Pareto front in Fig. 4a.

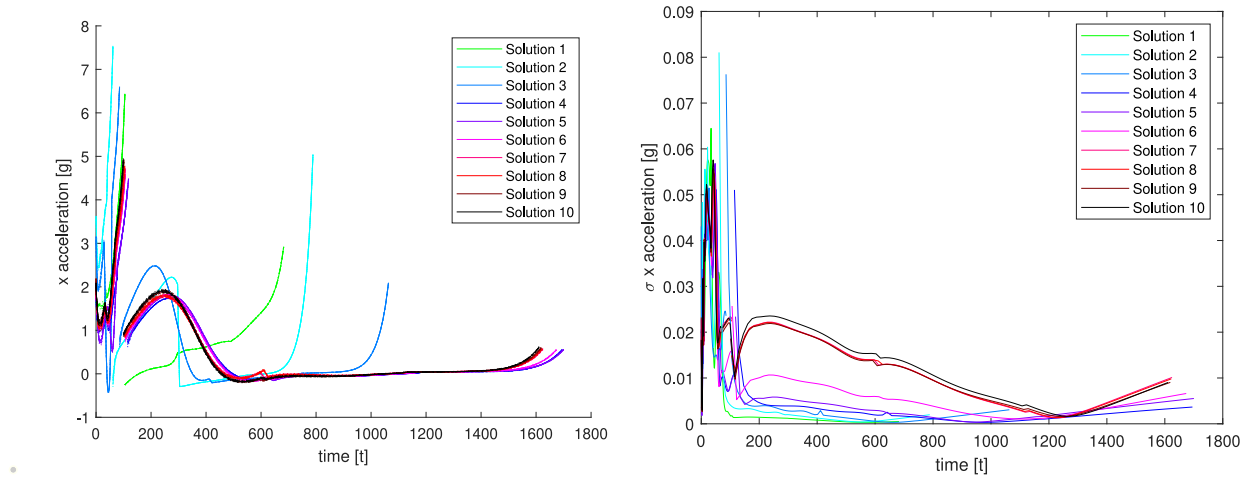

(a) (b)

Fig. 9 Time-history of a) the axial acceleration and b) its standard deviation, for each of the 10 solutions in the Pareto front in Fig. 4a.

References

[1] Wang, S., Li, Q., and Savage, G. J., "Reliability-based robust design optimization of structures considering uncertainty in design variables," *Mathematical Problems in Engineering*, Vol. 2015, 2015.

[2] Vasile, M., "Optimising resilience: at the edge of computability," *Mathematics Today*, Vol. 53, No. 5, 2017, pp. 231–234.

[3] Maddock, C., Toso, F., Ricciardi, L., Mogavero, A., Lo, K. H., Rengarajan, S., Kontis, K., Milne, A., Evans, D., West, M., et al., "Vehicle and mission design of a future small payload launcher," *21st AIAA International Space Planes and Hypersonics Technologies Conference*, 2017, p. 2224.

[4] Maddock, C. A., Ricciardi, L., West, M., West, J., Kontis, K., Rengarajan, S., Evans, D., Milne, A., and McIntyre, S., "Conceptual design analysis for a two-stage-to-orbit semi-reusable launch system for small satellites," *Acta Astronautica*, Vol. 152, 2018, pp. 782–792.

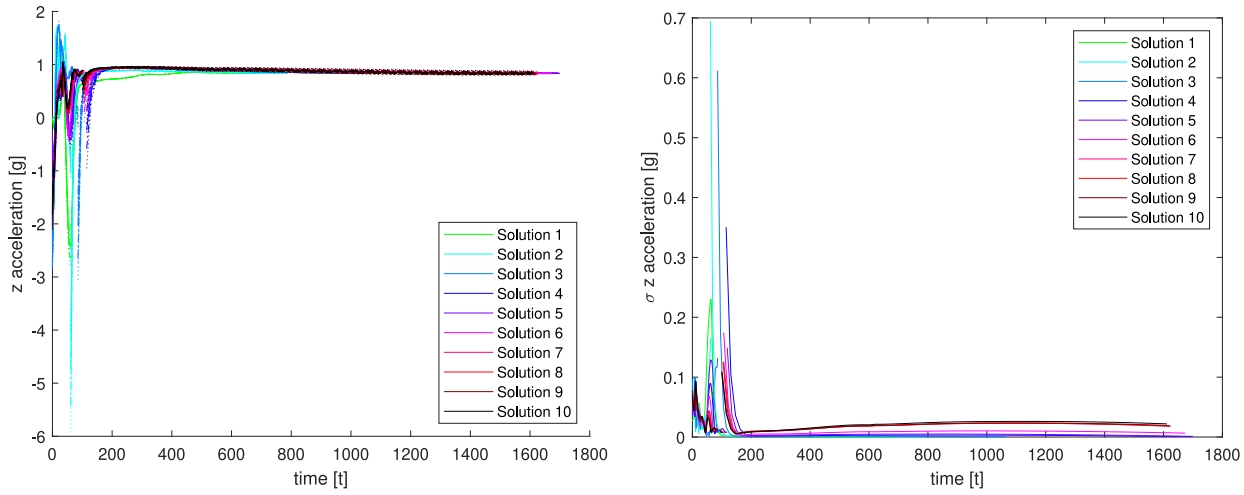

(a) (b)

Fig. 10 Time-history of a) the normal acceleration and b) its standard deviation, for each of the 10 solutions in the Pareto front in Fig. 4a.

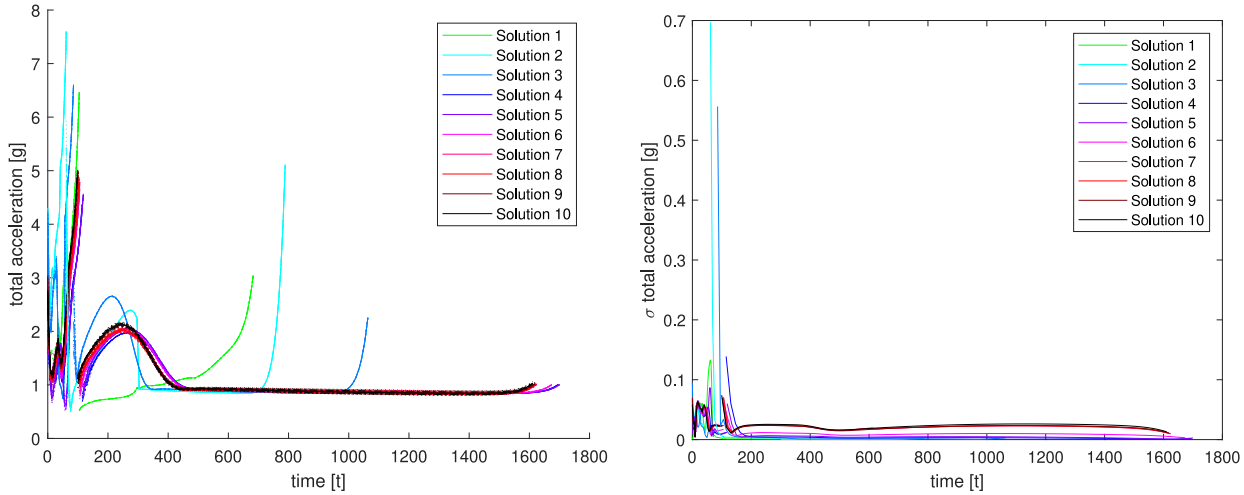

(a) (b)

Fig. 11 Time-history of a) the total acceleration and b) its standard deviation, for each of the 10 solutions in the Pareto front in Fig. 4a.

[5] McIntyre, S., Fawcett, T., Dickinson, T., West, M., Maddock, C. A., Mogavero, A., Ricciardi, L., Toso, F., Kontis, K., Lo, K. H., et al., "A commercially driven design approach to UK future small payload launch systems," *14th Reinventing Space Conference*, 2016.

[6] Ricciardi, L. A., Vasile, M., and Maddock, C., "Global solution of multi-objective optimal control problems with multi agent collaborative search and direct finite elements transcription," *2016 IEEE Congress on Evolutionary Computation (CEC)*, IEEE, 2016, pp. 869–876.

[7] Ricciardi, L. A., Maddock, C. A., and Vasile, M., "Direct solution of multi-objective optimal control problems applied to spaceplane mission design," *Journal of Guidance, Control, and Dynamics*, Vol. 42, No. 1, 2018, pp. 30–46.

[8] Vasile, M., "Finite Elements in Time: A Direct Transcription Method for Optimal Control Problems," *AIAA/AAS Astrodynamics Specialist Conference, Guidance, Navigation, and Control and Co-located Conferences*, Toronto, Canada, 2-5 Aug 2010. doi:0.2514/6.2010-8275.

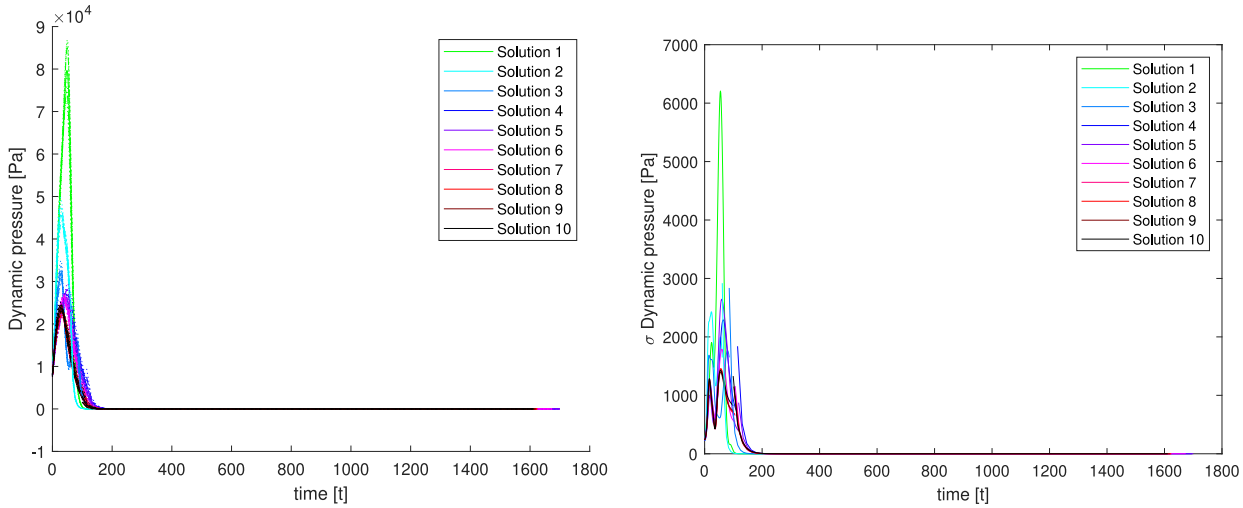

(a) (b)

Fig. 12 Time-history of a) the dynamic pressure and b) its standard deviation, for each of the 10 solutions in the Pareto front in Fig. 4a.

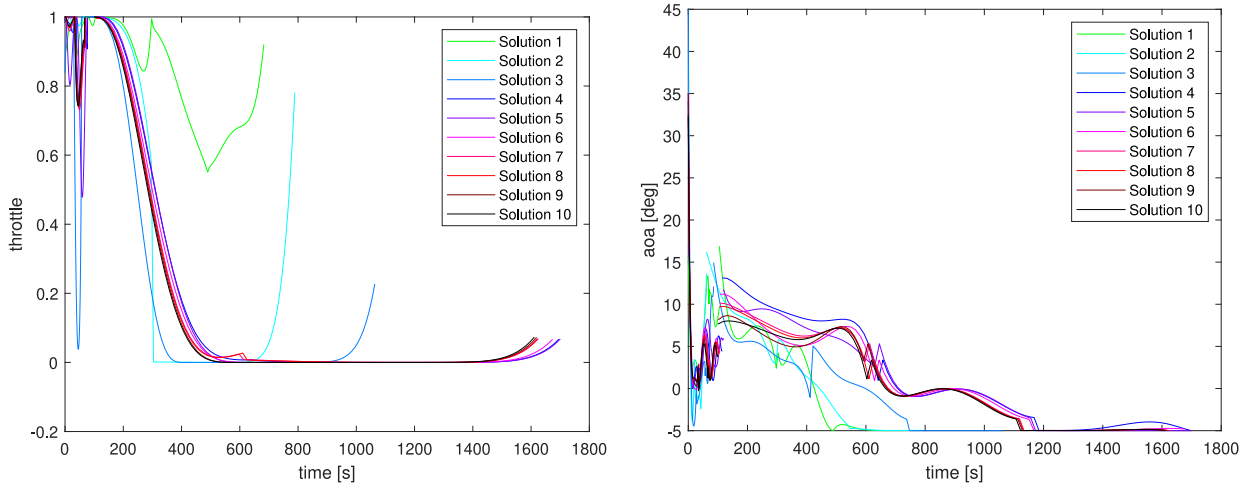

(a) (b)

Fig. 13 Time-history of a) the throttle and b) the angle of attack, for each of the 10 solutions in the Pareto front in Fig. 4a.

[9] Ricciardi, L. A., and Vasile, M., "Improved archiving and search strategies for Multi Agent Collaborative Search," *International Conference on Evolutionary and Deterministic Methods for Design, Optimization and Control with Applications to Industrial and Societal Problems (EUROGEN)*, Glasgow, UK, 14-16 Sep 2015.

[10] Ricciardi, L. A., Vasile, M., Toso, F., and Maddock, C. A., "Multi-objective optimal control of the ascent trajectories of launch vehicles," *AIAA/AAS Astrodynamics Specialist Conference*, 2016, p. 5669.

[11] Vasile, M. L., Maddock, C., and Ricciardi, L., "Multi-objective optimal control of re-entry and abort scenarios," *2018 Space Flight Mechanics Meeting*, 2018, p. 0218.

[12] Di Carlo, M., Ricciardi, L., and Vasile, M., "Multi-objective optimisation of constellation deployment using low-thrust propulsion," *AIAA/AAS Astrodynamics Specialist Conference*, 2016, p. 5577.

[13] Zuiani, F., Kawakatsu, Y., and Vasile, M., "Multi-objective optimisation of many-revolution, low-thrust orbit raising for Destiny mission," *23rd AAS/AIAA Space Flight Mechanics Conference*, Kauai, Hawaii, 10-14 Feb 2013.

[14] Ricciardi, L., Maddock, C., Vasile, M., Stindt, T., Merrifield, J., Fossati, M., West, M., Kontis, K., Farkin, B., and McIntyre, S., "Robust multi-objective optimisation of a descent guidance strategy for a TSTO spaceplane," *International Conference on Flight vehicles, Aerothermodynamics and Re-entry Missions and Engineering (FAR)*, 2019.

[15] Ross, I. M., Proulx, R. J., Karpenko, M., and Gong, Q., "Riemann–Stieltjes optimal control problems for uncertain dynamic systems," *Journal of Guidance, Control, and Dynamics*, Vol. 38, No. 7, 2015, pp. 1251–1263.

[16] der Merwe, R. V., and Wan, E. A., "The square-root unscented Kalman filter for state and parameter-estimation," *2001 IEEE International Conference on Acoustics, Speech, and Signal Processing Proceedings (Cat. No.01CH37221)*, IEEE, ???? doi:10.1109/icassp.2001.940586, URL https://doi.org/10.1109/icassp.2001.940586.

[17] Maddock, C., Ricciardi, L., Toso, F., and Vasile, M., "Multidisciplinary design analysis of a semi-reusable two-stage-to-orbit small payload launch system," *International Astronautical Congress (IAC)*, 2019.

[18] McIntyre, S., Fawcett, T., Dickinson, T., Maddock, C. A., Mogavero, A., Ricciardi, L., Toso, F., West, M., Kontis, K., Lo, K. H., et al., "How to launch small payloads? Evaluation of current and future small payload launch systems," *14th Reinventing Space Conference*, 2016.

[19] Zipfel, P., *Modeling and Simulation of Aerospace Vehicle Dynamics, Second Edition*, AIAA Education Series, 2007. doi:10.2514/4.862182.

[20] Stindt, T., Merrifield, J., Fossati, M., Ricciardi, L., Maddock, C., West, M., Kontis, K., Farkin, B., and McIntyre, S., "Aerodynamic database development for a future reusable space launch vehicle," *International Conference on Flight vehicles, Aerothermodynamics and Re-entry Missions and Engineering (FAR)*, 2019.

[21] NOAA, N., and Force, U. A., "US Standard Atmospheres," *Washington, DC: US Government Printing Office*, 1976, pp. 53–63.

[22] Picone, J. M., Hedin, A. E., Drob, D. P., and Aikin, A. C., "NRLMSISE-00 empirical model of the atmosphere: Statistical comparisons and scientific issues," *Journal of Geophysical Research: Space Physics*, Vol. 107, No. A12, 2002. doi: 10.1029/2002ja009430, URL https://doi.org/10.1029/2002ja009430.